Enhanced imaging of choroidal vasculature by high-penetration and dual-velocity optical coherence angiography

Franck Jaillon,[1] Shuichi Makita,[1] Eun-Jung Min,[2] Byeong Ha Lee,[2] and Yoshiaki Yasuno[1,*]

[1]*Computational Optics Group in the University of Tsukuba, 1-1-1 Tennodai, Tsukuba, Ibaraki 305-8573, Japan*
[2]*School of Information & Communications, Institute of Science and Technology, Gwangju, Korea*
**yasuno@optlab2.bk.tsukuba.ac.jp*

Abstract: Dual-beam-scan Doppler optical coherence angiography (DB-OCA) with a 1-μm-wavelength probe is demonstrated for improved *in vivo* choroidal angiograms of the human eye. This method utilizes two scanning beams with spatial and temporal separation on the retina, and provides two measurable velocity ranges. The method achieves higher sensitivity to very low velocity flows than conventional Doppler optical coherence tomography. Moreover, longer wavelengths allowing greater penetration, enhanced visualization of choroidal vessels is verified with *en-face* projection images of the Doppler shift squared. Specifically, better choroidal vasculature visibility is achieved at a wavelength of 1 μm than at 840 nm.

OCIS codes: (170.4500) Optical coherence tomography; (170.4470) Ophthalmology; (170.3880)

References and links

1. J. E. Grunwald, T. I. Metelitsina, J. C. Dupont, G. S. Ying, and M. G. Maguire, "Reduced foveolar choroidal blood flow in eyes with increasing AMD severity," Invest. Ophthalmol. Vis. Sci. **46**(3), 1033–1038 (2005).
2. L. A. Yannuzzi, K. T. Rohrer, L. J. Tindel, R. S. Sobel, M. A. Costanza, W. Shields, and E. Zang, "Fluorescein angiography complication survey," Ophthalmology **93**(5), 611–617 (1986).
3. U. Karhunen, C. Raitta, and R. Kala, "Adverse reactions to fluorescein angiography," Acta Ophthalmol. (Copenh.) **64**(3), 282–286 (1986).
4. C. Riva, B. Ross, and G. B. Benedek, "Laser Doppler measurements of blood flow in capillary tubes and retinal arteries," Invest. Ophthalmol. **11**(11), 936–944 (1972).
5. M. D. Stern, D. L. Lappe, P. D. Bowen, J. E. Chimosky, G. A. Holloway, Jr., H. R. Keiser, and R. L. Bowman, "Continuous measurement of tissue blood flow by laser-Doppler spectroscopy," Am. J. Physiol. **232**(4), H441–H448 (1977).
6. D. Huang, E. A. Swanson, C. P. Lin, J. S. Schuman, W. G. Stinson, W. Chang, M. R. Hee, T. Flotte, K. Gregory, C. A. Puliafito, and J. G. Fujimoto, "Optical coherence tomography," Science **254**(5035), 1178–1181 (1991).
7. A. F. Fercher, C. K. Hitzenberger, G. Kamp, and S. Y. El-Zaiat, "Measurement of intraocular distances by backscattering spectral interferometry," Opt. Commun. **117**(1-2), 43–48 (1995).
8. X. J. Wang, T. E. Milner, and J. S. Nelson, "Characterization of fluid flow velocity by optical Doppler tomography," Opt. Lett. **20**(11), 1337–1339 (1995).
9. J. A. Izatt, M. D. Kulkarni, S. Yazdanfar, J. K. Barton, and A. J. Welch, "In vivo bidirectional color Doppler flow imaging of picoliter blood volumes using optical coherence tomography," Opt. Lett. **22**(18), 1439–1441 (1997).
10. Z. Chen, T. E. Milner, D. Dave, and J. S. Nelson, "Optical Doppler tomographic imaging of fluid flow velocity in highly scattering media," Opt. Lett. **22**(1), 64–66 (1997).
11. Y. Zhao, Z. Chen, C. Saxer, S. Xiang, J. F. de Boer, and J. S. Nelson, "Phase-resolved optical coherence tomography and optical Doppler tomography for imaging blood flow in human skin with fast scanning speed and high velocity sensitivity," Opt. Lett. **25**(2), 114–116 (2000).
12. R. A. Leitgeb, L. Schmetterer, C. K. Hitzenberger, A. F. Fercher, F. Berisha, M. Wojtkowski, and T. Bajraszewski, "Real-time measurement of in vitro flow by Fourier-domain color Doppler optical coherence tomography," Opt. Lett. **29**(2), 171–173 (2004).

#143472 - $15.00 USD Received 1 Mar 2011; revised 6 Apr 2011; accepted 6 Apr 2011; published 11 Apr 2011

13. R. M. Werkmeister, N. Dragostinoff, M. Pircher, E. Götzinger, C. K. Hitzenberger, R. A. Leitgeb, and L. Schmetterer, "Bidirectional Doppler Fourier-domain optical coherence tomography for measurement of absolute flow velocities in human retinal vessels," Opt. Lett. **33**(24), 2967–2969 (2008).
14. L. Yu and Z. Chen, "Doppler variance imaging for three-dimensional retina and choroid angiography," J. Biomed. Opt. **15**(1), 016029 (2010).
15. S. Makita, Y. Hong, M. Yamanari, T. Yatagai, and Y. Yasuno, "Optical coherence angiography," Opt. Express **14**(17), 7821–7840 (2006).
16. Y. Hong, S. Makita, M. Yamanari, M. Miura, S. Kim, T. Yatagai, and Y. Yasuno, "Three-dimensional visualization of choroidal vessels by using standard and ultra-high resolution scattering optical coherence angiography," Opt. Express **15**(12), 7538–7550 (2007).
17. Y. Yasuno, Y. Hong, S. Makita, M. Yamanari, M. Akiba, M. Miura, and T. Yatagai, "In vivo high-contrast imaging of deep posterior eye by 1-μm swept source optical coherence tomography and scattering optical coherence angiography," Opt. Express **15**(10), 6121–6139 (2007).
18. A. H. Bachmann, M. L. Villiger, C. Blatter, T. Lasser, and R. A. Leitgeb, "Resonant Doppler flow imaging and optical vivisection of retinal blood vessels," Opt. Express **15**(2), 408–422 (2007).
19. J. Fingler, R. J. Zawadzki, J. S. Werner, D. Schwartz, and S. E. Fraser, "Volumetric microvascular imaging of human retina using optical coherence tomography with a novel motion contrast technique," Opt. Express **17**(24), 22190–22200 (2009).
20. L. An and R. K. Wang, "In vivo volumetric imaging of vascular perfusion within human retina and choroids with optical micro-angiography," Opt. Express **16**(15), 11438–11452 (2008).
21. T. Schmoll, C. Kolbitsch, and R. A. Leitgeb, "Ultra-high-speed volumetric tomography of human retinal blood flow," Opt. Express **17**(5), 4166–4176 (2009).
22. Y. K. Tao, K. M. Kennedy, and J. A. Izatt, "Velocity-resolved 3D retinal microvessel imaging using single-pass flow imaging spectral domain optical coherence tomography," Opt. Express **17**(5), 4177–4188 (2009).
23. A. Szkulmowska, M. Szkulmowski, D. Szlag, A. Kowalczyk, and M. Wojtkowski, "Three-dimensional quantitative imaging of retinal and choroidal blood flow velocity using joint Spectral and Time domain Optical Coherence Tomography," Opt. Express **17**(13), 10584–10598 (2009).
24. I. Gorczynska, D. Szlag, M Szkulmowski, D. Bukowska, I. Grulkowski, A.A. Kowalczyk, and M. Wojtkowski, "Velocity ranging in joint spectral and time domain OCT imaging with resonant scanner," presented at Photonics West, San Francisco, USA, Jan. 22–27, 2011.
25. P. Meemon and J. P. Rolland, "Swept-source based, single-shot, multi-detectable velocity range Doppler optical coherence tomography," Biomed. Opt. Express **1**(3), 955–966 (2010).
26. S. Makita, F. Jaillon, M. Yamanari, M. Miura, and Y. Yasuno, "Comprehensive in vivo micro-vascular imaging of the human eye by dual-beam-scan Doppler optical coherence angiography," Opt. Express **19**(2), 1271–1283 (2011).
27. S. Makita, M. Yamanari, and Y. Yasuno, "High-speed and high-sensitive optical coherence angiography," Proc. SPIE **7372**, 73721M, 73721M-6 (2009).
28. S. Zotter, M. Pircher, T. Torzicky, M. Bonesi, E. Götzinger, R. A. Leitgeb, and C. K. Hitzenberger, "Visualization of microvasculature by dual-beam phase-resolved Doppler optical coherence tomography," Opt. Express **19**(2), 1217–1227 (2011).
29. E. C. W. Lee, J. F. de Boer, M. Mujat, H. Lim, and S. H. Yun, "In vivo optical frequency domain imaging of human retina and choroid," Opt. Express **14**(10), 4403–4411 (2006).
30. B. Povãzay, K. Bizheva, B. Hermann, A. Unterhuber, H. Sattmann, A. Fercher, W. Drexler, C. Schubert, P. Ahnelt, M. Mei, R. Holzwarth, W. Wadsworth, J. Knight, and P. S. J. Russell, "Enhanced visualization of choroidal vessels using ultrahigh resolution ophthalmic OCT at 1050 nm," Opt. Express **11**(17), 1980–1986 (2003).
31. B. H. Park, M. C. Pierce, B. Cense, S.-H. Yun, M. Mujat, G. J. Tearney, B. E. Bouma, and J. F. de Boer, "Real-time fiber-based multi-functional spectral-domain optical coherence tomography at 1.3 microm," Opt. Express **13**(11), 3931–3944 (2005).
32. C. Kasai, K. Namekawa, A. Koyano, and R. Omoto, "Real-time two-dimensional blood flow imaging using an autocorrelation technique," IEEE Trans. Sonics Ultrason. **SU-32**, 458–464 (1985).
33. V. X. D. Yang, M. L. Gordon, A. Mok, Y. Zhao, Z. Chen, R. S. C. Cobbold, B. C. Wilson, and A. Vitkin, "Improved phase-resolved optical Doppler tomography using the Kasai velocity estimator and histogram segmentation," Opt. Commun. **208**(4-6), 209–214 (2002).
34. S. Jiao and L. V. Wang, "Jones-matrix imaging of biological tissues with quadruple-channel optical coherence tomography," J. Biomed. Opt. **7**(3), 350–358 (2002).
35. M. Yamanari, S. Makita, V. D. Madjarova, T. Yatagai, and Y. Yasuno, "Fiber-based polarization-sensitive Fourier domain optical coherence tomography using B-scan-oriented polarization modulation method," Opt. Express **14**(14), 6502–6515 (2006).

1. Introduction

Imaging choroidal vasculature is essential to understanding choroidal vascularization abnormalities of eye pathologies. For example, it has been shown that the severity of age-

#143472 - $15.00 USD Received 1 Mar 2011; revised 6 Apr 2011; accepted 6 Apr 2011; published 11 Apr 2011

related macular degeneration (AMD) is characterized by a systematic decrease in foveolar choroidal blood flow [1]. Current standard technique to image choroidal vasculature is indocyanine green angiography (ICGA). ICGA gives qualitative and functional information and may involve patient discomfort since it requires dye injection, which has the potential to induce adverse reactions [2,3]. Laser Doppler flowmetry (LDF) is another method to obtain blood flow in absolute units [4,5]. LDF produces vasculature images but it does not give depth information, that is, it cannot be known whether vessels belong to retina or choroid.

Optical coherence tomography (OCT) [6] is a noninvasive, noncontact imaging technique for micrometer-scale, three-dimensional (3D) retinal tomography. Spectral-domain OCT (SD-OCT) [7] has a better acquisition rate than time-domain OCT. In addition, similar to time-domain OCT [8–10], in SD-OCT, flow information can be acquired via the Doppler OCT method [11–14].

Since the first demonstration of Doppler OCT, various improved versions have been reported. Optical coherence angiography (OCA) [15] is a set of hardware and software methods for enhanced visualization of retinal and choroidal vasculature; OCA includes motion compensation and segmentation algorithms and is based on Doppler OCT [15] and intensity-based segmentation [16,17]. Another method for enhanced visualization of ocular vasculature based on OCT is resonant Doppler Fourier-domain OCT [18], which uses an electro-optical phase modulator to enhance the blood flow contrast with respect to static structures. It has also been proposed a motion contrast technique to image a larger range of velocities [19]. Optical micro-angiography (OMAG) is another angiography method based on OCT that has demonstrated enhanced contrast for retinal perfusion [20]. Ultra-high-speed Doppler SD-OCT was demonstrated using CMOS technology [21]. Single-pass flow imaging spectral-domain OCT [22] and joint spectral- and time-domain OCT [23,24] are other techniques that improve vasculature imaging of the human eye. Lately, it has been reported that a system based on swept-source OCT with multiple detectable velocity ranges can achieve enhanced slow-flow sensitivity [25].

We previously proposed dual-beam-scan Doppler optical coherence angiography (DB-OCA) [26,27] as a method for enhanced vasculature imaging. Note that another group has recently used dual-beam method to obtain vasculature imaging [28]. In general, the ability of Doppler OCT to detect low-velocity vessels diminishes as the acquisition rate increases. DB-OCA avoids this tradeoff by employing two spatially separated probing beams. And it gives access to both high and low velocities without sacrificing the acquisition rate. This makes it possible to detect slow-flow structures with a high-speed acquisition system.

In this paper, we demonstrate highly sensitive and penetrating imaging of choroidal vasculature employing DB-OCA and a 1-μm probe beam, which has recently attracted interest owing to its high penetration into the deep choroid [29,30]. We first discuss the limitations of conventional Doppler SD-OCT, and then briefly present the principle of DB-OCA. A newly developed dual-beam-scan Doppler OCA system employing a 1-μm probe beam is then described. Enhanced contrast imaging of *in vivo* human choroidal vasculature is demonstrated. Finally, DB-OCA results obtained with an 840-nm probe and 1-μm probe are compared.

2. Principle

2.1. Conventional Doppler OCT and its limitations

In conventional phase-resolved Doppler OCT [11], velocity information for regions within the sample is retrieved by introducing a phase difference between adjacent A-lines. This phase difference $\Delta\phi$ is related to the axial velocity v_z via

$$v_z = \frac{\lambda_0 \Delta\phi}{4\pi\, n t_A}, \tag{1}$$

#143472 - $15.00 USD Received 1 Mar 2011; revised 6 Apr 2011; accepted 6 Apr 2011; published 11 Apr 2011

where λ_0 is the source center wavelength, n is the refractive index of the tissue, and t_A is the time separation between adjacent A-lines, which is inversely proportional to the charge-coupled device (CCD) acquisition rate. According to the phase sensitivity of OCT and the 2π ambiguity of phase (i.e., $-\pi < \Delta\phi \le \pi$), the range of detectable velocities is given by [31]

$$\frac{\lambda_0}{4\pi n\, t_A}\sqrt{\frac{1}{SNR}+\sigma_{\Delta x}} \le |v_z| \le \frac{\lambda_0}{4nt_A}, \tag{2}$$

where SNR is the signal-to-noise ratio (SNR), and $\sigma_{\Delta x}$ is the phase noise arising from decorrelation between adjacent A-lines and is defined as

$$\sigma_{\Delta x} = \sqrt{\frac{4\pi}{3}\left(1-\exp\left(-\frac{1}{2}\left(\frac{\Delta x}{r}\right)^2\right)\right)}, \tag{3}$$

where r is the beam radius on the sample and Δx is the distance between adjacent A-lines. In general, a high acquisition rate, equivalent to small t_A, is required for less sensitivity to motion artifacts. However, according to Eq. (2) with given SNR and $\sigma_{\Delta x}$, small t_A implies that the velocity range shifts to high velocities. Consequently, slow-flow structures will not be detected. To resolve this issue, we propose DB-OCA [26], whose principle is described in the next section.

2.2. Dual-beam-scan Doppler OCA

Figure 1 illustrates the principle of DB-OCA, where the sample is scanned by two beams, beam-1 and beam-2, having the same scanning speed. Their spatial separation d is thus a constant. This separation d is the product of the scanning step size and an integer p. The time separation is thus $T = p.t_A$, with t_A being the acquisition time of a single A-line. Beam-2 is at the same lateral position as beam-1 after the delay T. Therefore, the B-scan obtained with beam-2 is laterally shifted with respect to that obtained with beam-1. Consequently, at a given depth z, the phase of beam-2, $\varphi_2(z, t + T)$, acquired at time $t + T$ is subtracted from the phase $\varphi_1(z, t)$ of beam-1 acquired at time t. Indeed, it corresponds to the phase difference obtained at the same lateral position but acquired at a different moment. The axial velocity of the conventional Doppler equation (Eq. (1)) is therefore rewritten as

$$v_z = \frac{\lambda_0\left[\phi_1(z,t)-\phi_2(z,t+T)\right]}{4\pi\, n\, T}. \tag{4}$$

From Eq. (4) and Ref. 31, the velocity range of DB-OCA is then given by

$$\frac{\lambda_0}{4\pi n\, T}\sqrt{\frac{1}{SNR}} \le |v_z| \le \frac{\lambda_0}{4nT}\ . \tag{5}$$

#143472 - $15.00 USD Received 1 Mar 2011; revised 6 Apr 2011; accepted 6 Apr 2011; published 11 Apr 2011

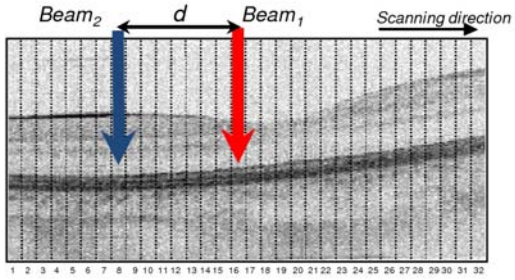

Fig. 1. Dual-beam-scan Doppler OCA: two beams scan the sample with a constant spatial separation *d*.

From Eq. (5), we see that this technique using two beams allows the measurement of vessels with low-velocity flow since $t_A < T$. It is noteworthy that this low-velocity sensitivity is achieved without decreasing the acquisition rate. The minimum detectable velocity depends on *SNR* but not on the spatial separation between adjacent A-lines. Indeed, in DB-OCA, phases that are compared are measured at the same lateral position. Therefore, the flow sensitivity is improved.

In addition, the data processing method of conventional Doppler OCT described in section 2.1 can be applied to the OCT data set obtained for DB-OCA. This additional signal processing gives access to high-velocity flow. Consequently, the combination of DB-OCA and conventional Doppler OCT processing enables simultaneous visualization of low- and high-velocity vessels.

3. Method

In this section, we present the experimental setup of DB-OCA employing a 1-μm probe beam.

3.1. System hardware

The hardware scheme of DB-OCA is shown in Fig. 2. A broadband superluminescent diode (SLD) light source (Superlum, Ireland) with a center wavelength of 1020 nm and a spectral width (FWHM) of 100 nm was employed. This spectral width results in a measured axial resolution of 6 μm in air. Considering the refractive index of tissue (n = 1.38), the axial resolution in tissue is estimated to be 4.4 μm. The light is transmitted through a single-mode fiber to an isolator. After the isolator, a single-mode fiber delivers the light to a polarization-maintaining (PM) fiber-based coupler (50/50) (General Photonics, CA). A polarization controller is positioned before the PM fiber coupler so that the two polarization channels of the PM fiber have identical power. A variable neutral density filter (VNF) is placed at the reference arm to optimize the sensitivity as close as possible to the shot-noise limit.

The sample arm consists of a specially designed scanning head described in Fig. 3. In the scanning head, the two orthogonal states of polarization (SOPs) of the PM fiber are separated by a Wollaston prism (Halbo Optics, UK). The two beams with different SOPs are relayed by two achromatic lenses (f = 60 and 75 mm) and deflected by X–Y galvanometers. By means of an achromatic lens (f = 60 mm) and an ophthalmic lens (40D, Volk, Mentor, OH), the beams reach the cornea with different incident angles. The incident power on the cornea is 1.6 mW. The two beams have a spatial separation d on the retina of 162 μm. They are then backscattered by the retina and recombined by the Wollaston prism.

The probe beams interfere with the reference beam in the fiber coupler. A fiber-based polarizing beam splitter (PBS) (General Photonics, Chino, CA) then separates the two SOPs into two beams and the two beams are directed to different spectrometers, which share an

#143472 - $15.00 USD Received 1 Mar 2011; revised 6 Apr 2011; accepted 6 Apr 2011; published 11 Apr 2011

identical design. Each spectrometer consists of a fiber tip collimator, a blazed grating (1200 lp/mm, Thorlabs, NJ), an achromatic lens pair (f = 200 and 150 mm, assembled into a composite lens with f = 88 mm), and a high-speed InGaAs scan camera (1024 pixels, 46.9 kHz line rate, SU1024LDH-1.7RT-0500LC, Sensors Unlimited Inc., Goodrich, NJ). The OCT sensitivities measured with the spectrometers were 96.0 and 95.6 dB. The spectral interference signal is acquired through a Camera Link frame grabber board (PCIe-1430, National Instruments, TX). The data acquisition of both CCD cameras and the scanning of the galvanometers were synchronized via control signals generated by a function generator board (PCI-6713, National Instruments, TX) built into a standard personal computer (PC).

Owing to mismatch of PM fiber lengths between sample and reference arms, there is a difference between optical pathlengths of the two SOPs. This creates an axial displacement between the two OCT signals. This axial displacement is estimated using a static phantom and by numerically shifting the two B-scans in the axial direction. The optimal shift is achieved when the variance of the phase difference between two OCT signals is minimal. Typically, the variance has been computed over a B-scan area containing 100,000 pixels. Note that the variance is the energy of the phase error, and this should take its minimum when the axial displacement is zero. Moreover, to align the two spectrometers, we blocked the sample arm and placed a glass slide in front of the mirror of the reference arm. This configuration is similar to that of a Fizeau interferometer. By doing so and then by minimizing the phase difference for all depths between the two OCT signals of the two polarization channels, we could effectively align the spectrometers.

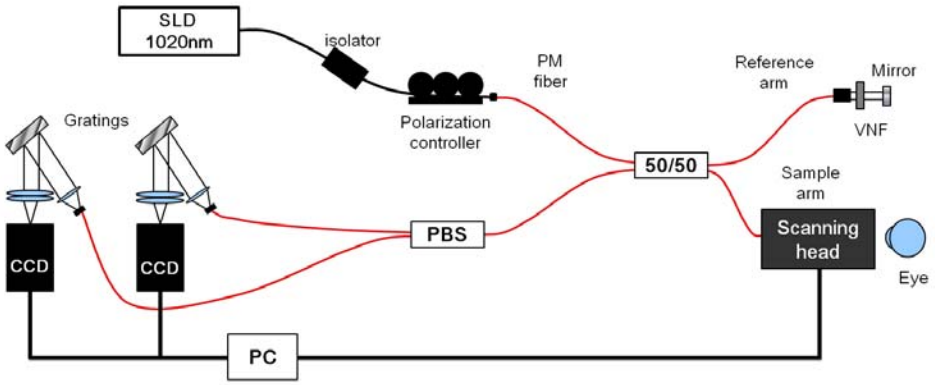

Fig. 2. Schematic diagram of the dual-beam-scan Doppler OCA setup. VNF: variable neutral density filter. Red lines are polarization-maintaining (PM) fibers. CCD: coupled charge device, PBS: polarization beam splitter.

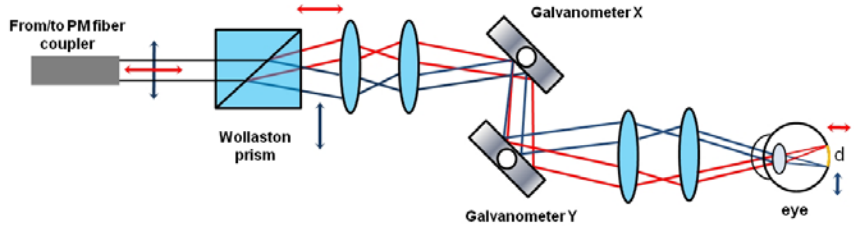

Fig. 3. , Scanning head: Two polarization states (red and blue) are separated by a Wollaston prism. After passing through relay lenses and galvanometers, the two polarization states reach the retina with a spatial separation d.

#143472 - $15.00 USD Received 1 Mar 2011; revised 6 Apr 2011; accepted 6 Apr 2011; published 11 Apr 2011

3.2. Velocity computation

As described in the previous section, two spectra are acquired by the DB-OCA system. Standard SD-OCT processing including rescaling and Fourier transformation yields two complex OCT signals, $\Gamma_1(i,j)$ and $\Gamma_2(i,j)$, where the axial position (depth) is given by the index *i* and the lateral position (time) by the index *j*.

3.2.1. Low-velocity images

First, to image low-velocity structures, we compute the phase shift $\Delta\phi_{i,j}$ between the two complex OCT signals at the position (*i*, *j*). Using Kasai autocorrelation [32,33], $\Delta\phi_{i,j}$ is defined as

$$\Delta\phi_{i,j} = Arg\left[\sum_{m=0}^{M-1}\sum_{n=0}^{N-1}\Gamma_1(i+m,\, j+n)\Gamma_2^{*}(i+m,\, j+n+p)\right], \tag{6}$$

where *M* and *N* are respectively the axial and lateral window sizes in units of pixels. Here *M* = 3 and *N* = 1. The integer *p* is the lateral shift between the two OCT signals caused by the spatial separation of the two probe beams, and defined by $p = T / t_A$. The Doppler shift Δf_S is then obtained as

$$\Delta f_S = \frac{1}{2\pi T}\Delta\phi_{i,j}. \tag{7}$$

In the following, we use the square of the Doppler shift Δf_S^2 to create en-face low-velocity images.

3.2.2. High-velocity images

To obtain a high-velocity flow image, we first compute the following expression at a given location (*i*, *j*):

$$\Gamma(i,j) = \Gamma_1(i,\, j)\Gamma_1^{*}(i,\, j+1) + \Gamma_2(i,\, j+p)\Gamma_2^{*}(i,\, j+p+1). \tag{8}$$

The phase shift is given by

$$\Delta\phi_{i,j} = Arg\left[\sum_{m=0}^{M-1}\sum_{n=0}^{N-1}\Gamma\ (i+m,\, j+n)\right], \tag{9}$$

where *M* and *N* are again the axial and lateral window sizes, respectively. Here *M* = 1 and *N* = 2. The Doppler shift Δf_F for high velocity is obtained as

$$\Delta f_F = \frac{1}{2\pi\, t_A}\Delta\phi_{i,j}\ . \tag{10}$$

Then, similar to low-velocity images, taking the square of the Doppler shift Δf_F^2 is used to produce en-face projection high-velocity images.

4. Experiment

4.1. Measurement Protocol

We imaged three 3D volumes of the healthy myopic right eye of an Asian male (25 years old). Three volumes at three locations were acquired: (1) macula, (2) between macula and optic nerve head (ONH), and (3) ONH. A fast-horizontal-scanning protocol with a scanning range of 3.07 mm (horizontal) × 3.07 mm (vertical) was employed. The scanning step size

#143472 - $15.00 USD Received 1 Mar 2011; revised 6 Apr 2011; accepted 6 Apr 2011; published 11 Apr 2011

Δx between A-lines was 3.2 μm. The number of A-lines was 950, and the number of B-scans was 256. The two B-scans corresponding to the two beams have the same number of A-lines but are laterally shifted. Therefore only overlapping A-lines are conserved. Non-overlapping A-lines are located at the beginning of the B-scan generated by the following beam and at the end of that generated by the preceding beam. The beam size ($1/e^2$) on the retina was simulated by ray-tracing (Zemax, Bellevue, WA) to be 12 μm, which gave a radius r of 6 μm.

According to the time interval between A-lines (t_A) of 22 μs and a typical SNR of 15 dB, Eqs. (2) and (3) give the theoretical velocity range of a high-velocity image as 2.4 mm/s < v_z < 8.4 mm/s.

The low-velocity range is calculated using Eq. (5). The separation of the two probe beams d is 162 μm, which corresponds to 50 lines. Therefore, the delay T is $50 \times t_A = 1.1$ ms. With the assumption of a typical SNR of 15 dB, the low-velocity range is estimated to be 0.01 mm/s < v_z < 0.17 mm/s.

4.2. Image presentation

The measured Doppler volume is split into retinal and choroidal volumes according to the position of the retinal pigment epithelium (RPE), where the RPE position has been identified from the corresponding OCT volume employing a segmentation algorithm described in Ref. 15. To demonstrate retinal and choroidal OCA, *en-face* projection (average over retina/choroid thickness) images of the Doppler shift squared (square of Eqs. (7) or (10)) are obtained. Δf_S^2 and Δf_F^2 are thresholded for display as described in Ref. 26.

As discussed above, DB-OCA gives two Doppler images with different velocity ranges. In the following sections, these two Doppler images are referred to as the high-velocity image (Δf_F^2) and low-velocity image (Δf_S^2).

4.3. Results

Figure 4 shows mosaics of high-velocity images (Fig. 4a) and low-velocity images (Fig. 4b); each mosaic consists of three patches obtained at the macula, ONH, and their center. Here strong signal (Δf_S^2, Δf_F^2) is indicated by white color.

Choroidal vasculature comprises choriocapillaris, mid-sized vessels and large vessels. It can be reasonably assumed that the flow velocity differs for vessels of different sizes. The high-velocity choroidal vasculature image (Fig. 4a) predominantly shows large vessels that can be associated with high-velocity flow. Along a given vessel, Δf_F^2 was not continuous (red circles). This discontinuity can be explained by an abrupt change in the axial orientation of the vessel or the existence of pulsatile flow inside the vessels. Note that, although the images presented are choroidal vessels, projections of the signals above the RPE or shadows of retinal vessels are seen (blue arrows).

Figure 4b is a low-velocity choroidal vasculature image. In comparison with the high-velocity image (Fig. 4a), smaller vessels are clearly visualized. Several small vessels are visualized with high contrast, especially around the ONH. Some vessels observed in high-velocity image (Fig. 4a) are not visible in the low-velocity image (Fig. 4b). It may be explained as follows: first, multiple phase wrapping generated by high-velocity flows will randomize Doppler signal and second, low-velocity vessels that were not visible in the high-velocity image will appear in the low-velocity image. Therefore the contrast of the high-velocity vessels is strongly reduced with respect to surrounding environment. Moreover, in order to optimize the display, the image dynamic ranges of Figs. 4(a) and (b) are not identical. Note that shadows (blue arrows) of retinal vessels appear with higher contrast than those in the high-velocity image owing to the higher flow sensitivity. Retinal vessels that are

#143472 - $15.00 USD Received 1 Mar 2011; revised 6 Apr 2011; accepted 6 Apr 2011; published 11 Apr 2011

responsible for these shadows are visualized by low-velocity images of the retinal vasculature (Fig. 5).

Strong Δf_S^2 can be seen at the ONH (yellow arrows) for low-velocity mosaics (Fig. 4b). It is conjectured that this higher signal may not be due to strong blood flow but an artifact of ocular birefringence. The sclera, which is known to have strong birefringence, is closer to the retinal surface in this region. Since DB-OCA uses polarization to multiplex two probe beams, the scleral birefringence results in cross-talk between the two probe beams. This cross-talk generates the strong artifact. The artifact can be reduced if circularly polarized incident light is used instead of linearly polarized light [34] as has been demonstrated with an 840-nm probe beam [27].

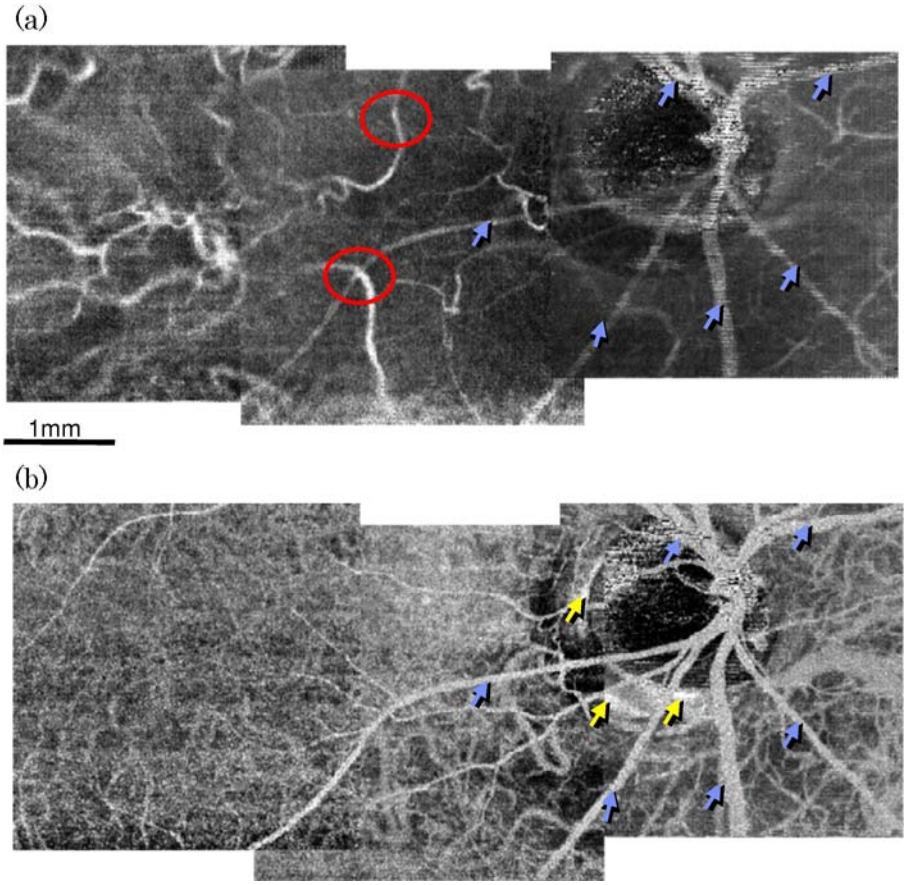

Fig. 4. Mosaic of high-velocity (a) and low-velocity (b) *en-face* images of choroidal vasculature. Location: from macula to the ONH. Inverted grayscale. The scale is the same for (a) and (b). See text for details.

In Fig. 6, a composite mosaic is realized by choosing a color depending on velocity and depth (retina/choroid). Low-velocity retinal vasculature is represented in red color. High-velocity choroidal vasculature is indicated in green color and low-velocity choroidal vasculature corresponds to inverted grayscale. An arbitrary threshold has been applied on low-velocity retinal and high-velocity choroidal vasculatures to enhance visualization. Note that the vasculature corresponding to the conventional Doppler (high-velocity) of the retina was hardly visible and is therefore not used here. The depth information given by DB-OCA enables to establish if vessels are really connected or simply overlaid. DB-OCA can thus distinguish vessels belonging to well-separated layers such as retina and choroid. As

#143472 - $15.00 USD Received 1 Mar 2011; revised 6 Apr 2011; accepted 6 Apr 2011; published 11 Apr 2011

previously observed, one limitation of the Doppler SD-OCT technique is the shadow artifact which is due to phase decorrelation below vessels. In B-scan or 3D representations, it can hinder visualization of vessels located below shallower vessels. Note also that in the case of pathological eyes, leakage cannot be directly detected by DB-OCA. Nevertheless, we have seen that 1-µm DB-OCA can provide complementary information about deep vasculature in a non-invasive and non-contact manner that is not available by conventional Doppler OCT.

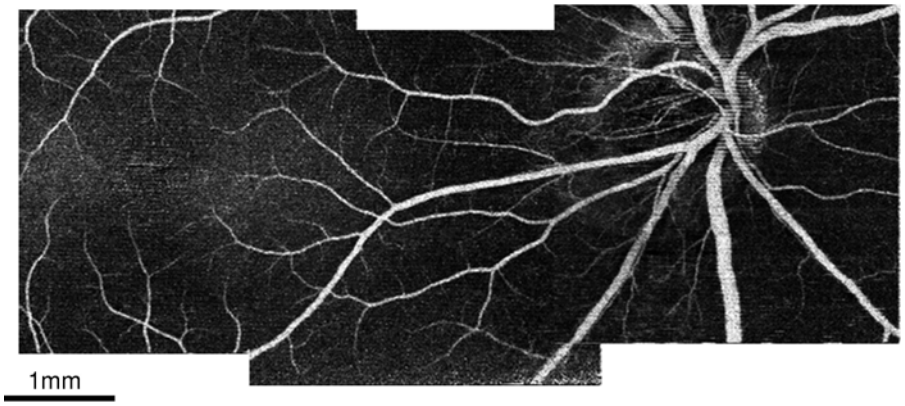

Fig. 5. Mosaic of low-velocity *en-face* images of retinal vasculature obtained from Δf_S^2 volumes. Location: from macula to the ONH. Inverted grayscale.

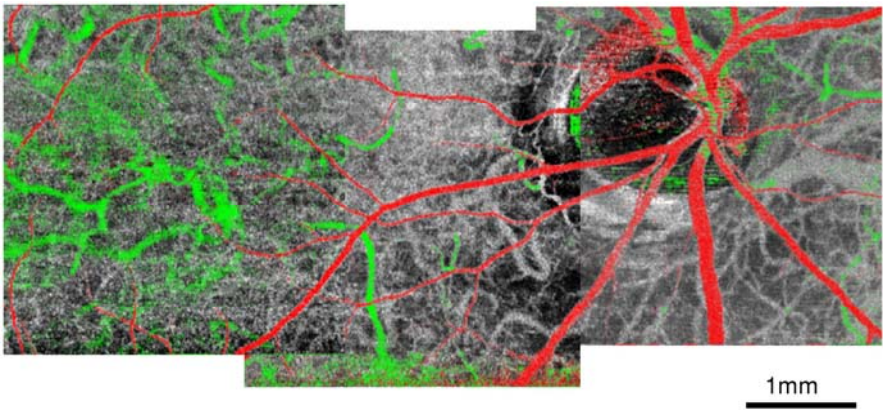

Fig. 6. Composite mosaic of low-velocity and high-velocity *en-face* images of retinal andchoroidal vasculature. Location: from macula to optic nerve head. Choroid low-velocity vasculature (inverted grayscale), choroid high-velocity vasculature (green), low-velocity retinal vasculature (red).

5. Discussion: Comparison of 840-nm and 1-µm DB-OCA

To evaluate the advantage of 1-µm DB-OCA, the low-velocity choroidal images of 840-nm and 1-µm DB-OCA are qualitatively compared. An 840-nm DB-OCA system described in Ref. 26 was employed for this comparison. Briefly, the light source was a superluminescent diode (SLD-37-HP, Superlum Diodes Ltd., Ireland) with 840-nm central wavelength and 50-nm bandwidth (full-width at half-maximum). The scanning head was identical to that of 1-µm DB-OCT system. The power on the cornea was 750 µW.

In the 840-nm DB-OCA, the spectral interference signals were acquired by a polarization diversity spectrometer [35], with a polarization beam splitter splitting the two polarization modes after a diffraction grating. Finally, two line-scan cameras (2048 pixels, 27.8 kHz;

#143472 - $15.00 USD Received 1 Mar 2011; revised 6 Apr 2011; accepted 6 Apr 2011; published 11 Apr 2011

AViiVA M2 CL 2014, e2V, Atmel, CA) detected the two polarization modes. The sensitivity was measured to be 94 dB and 93 dB for the two channels.

The 840-nm DB-OCA was configured to have the same maximum velocity as for the 1-μm DB-OCA. In this configuration, the temporal separation of the two probing beams was 0.905 ms. The reason why we selected a smaller temporal separation is to compensate for wavelength difference. From Eq. (5) and assuming similar refractive index for both wavelengths, we see that, in order to have the same velocity range and thus the same flow sensitivity, we need 840 nm/T_{840} = 1020 nm/T_{1020}, where T_{840} and T_{1020} are the delay between beams for corresponding wavelengths. Since T_{1020} = 1.1 ms, T_{840} = 0.905 ms. The lateral spatial separation of the retina was 170 μm, and the lateral separation in the image was 24 pixels. Hence, the scanning speed of the galvanometer scanner was configured to have a scanning step size of 7.07 μm between successive A-lines. Since a B-scan is configured to have 440 A-lines, the lateral scanning range was 3.10 mm. This is nearly identical to that of 1-μm DB-OCA of 3.07 mm.

Figure 7 shows *en-face* projection images of Δf_S^2 volumes obtained by 840-nm DB-OCA (a) and 1-μm DB-OCA (b). Here the projections were obtained by averaging Δf_S^2 signals through the whole depth including retina and choroid. The contrast of choroidal vessels in the 1-μm image is significantly higher than that in the 840-nm image. Furthermore, small choroidal vessels are better distinguished in the 1-μm image than in the 840-nm image. The superior performance of 1-μm DB-OCA is particularly evident in the region indicated by the yellow boxes. Since both systems were configured to have identical velocity range, this superior contrast is mainly attributable to the superior penetration of the 1-μm probe beam.

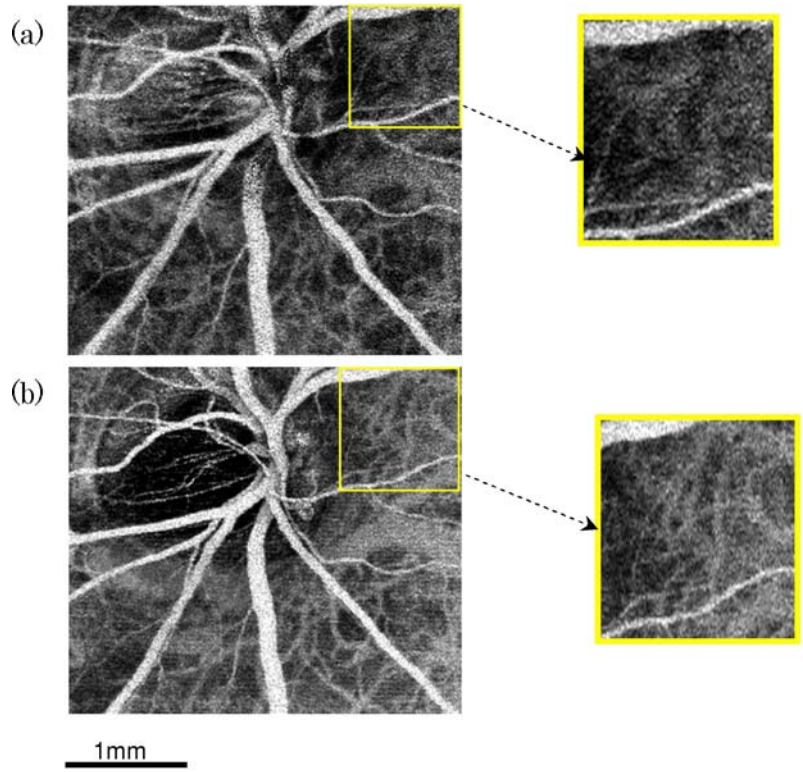

Fig. 7. *En-face* Δf_S^2 projection image of ONH for (a) 840-nm and (b) 1020-nm light sources. Yellow boxes are zoomed areas. Inverted grayscale.

#143472 - $15.00 USD Received 1 Mar 2011; revised 6 Apr 2011; accepted 6 Apr 2011; published 11 Apr 2011

6. Conclusion

We have demonstrated that 1-μm DB-OCA was particularly valuable for high-contrast imaging of choroidal vasculature. DB-OCA provided two angiograms that had different velocity ranges. High-velocity information was obtained with conventional phase- resolved Doppler method and low-velocity information was retrieved by using the phase difference between the two scanning beams. The low-velocity angiogram was found to have high flow sensitivity and to be undoubtedly useful for the visualization of small choroidal vessels. On the other hand, the high-velocity angiogram is important for the visualization of large choroidal vessels. The combination of the low- and high-velocity angiograms provides a more complete visualization of choroidal vasculature. An *in vivo* qualitative comparison of 840-nm and 1-μm DB-OCAs showed that 1-μm DB-OCA visualized the choroidal vessels with higher contrast. This non-invasive angiography may facilitate understanding and diagnosis of choroidal pathologies.

Acknowledgment

This study was partially supported by the Japan Science and Technology Agency through a contract for the Development of Systems and Technology for Advanced Measurement and Analysis.

#143472 - $15.00 USD Received 1 Mar 2011; revised 6 Apr 2011; accepted 6 Apr 2011; published 11 Apr 2011